

assumed from the edge of the SiO₂ conduction band corresponding to the energies of 3.04 and 2.76 eV for the HE region. We cannot surely find the appropriate energy levels for c-Si. These two energy levels also are observed in the oxidation process of hydrogenated amorphous Si (a-Si:H). Figure 7 shows the spectra of the emission light during the anodic oxidation of c-Si (solid line) and a-Si:H (dashed line), and aluminum (Al) metal. The a-Si:H film with a thickness greater than 300 nm was deposited on a c-Si substrate by a plasma chemical vapor deposition (CVD) method. The oxidation process of Al metal was carried out using the same method as in the case of Si oxidation except for the replacement of the electrolyte with a mixture of pure water, citric acid [1.5 weight percent (w/o)], and ammonium citrate (1.5 w/o). The spectrum recorded in the course of Al oxidation exhibits an emission peak only in the LE region. The spectra of a-Si:H and c-Si are almost similar. These experimental results suggest that the interface energy levels for light emission at the SiO₂-Si interface may be attributed to the creation of chemical bonding between the SiO₂ and Si, and they do not depend on the structure of Si.

Summary

The relation of light emission and anodic oxidation of c-Si have been studied. No light emission can be observed until the SiO₂ film grows to the thickness 15 nm. After reaching this critical value, the light emission appears and the integrated intensity of the light increases exponentially with SiO₂ film thickness having a factor of 10 nm. The spectrum of the emission light consists of different regions, i.e., LE and HE regions. The LE region has a broad peak corresponding to the energy of 1.93 eV and its intensity increases with the thickness of the SiO₂ film. The HE region exhibits two peaks of 3.04 and 2.76 eV, regardless of the thickness of

the SiO₂ film. A-Si:H also shows a similar spectrum. Therefore, the light emission in the LE region is attributed to the emission centers excited by hot electrons accelerated by the high field of about 22 MV/cm in the SiO₂ layer and in the HE region it is due to the interface levels resulting from the creation of chemical bonds between SiO₂ and Si.

Manuscript submitted Nov. 5, 1992; revised manuscript received Jan. 28, 1993.

Shizuoka University assisted in meeting the publication costs of this article.

REFERENCES

1. T. H. Ning and H. N. Yu, *J. Appl. Phys.*, **45**, 5373 (1974).
2. D. R. Young, *ibid.*, **47**, 2098 (1976).
3. J. F. Verwey, *ibid.*, **44**, 2681 (1973).
4. E. H. Nicollian and C. N. Berglund, *ibid.*, **41**, 3052 (1970).
5. R. Williams, *Phys. Rev.*, **140**, A569 (1965).
6. T. H. Ning, *Solid-State Electron.*, **21**, 273 (1978).
7. L. T. Canham, *Appl. Phys. Lett.*, **57**, 1046 (1990).
8. T. Ito, T. Ohta, and A. Hiraki, *Jpn. J. Appl. Phys.*, **31**, L1 (1992).
9. N. Koshida and H. Koyama, *Appl. Phys. Lett.*, **60**, Jan (1992).
10. *Light Emission from Silicon*, S. S. Iyer, R. T. Collins, and L. T. Canham, Editors, Material Research Society, Pittsburgh, PA (1992).
11. Y. Nakanishi, G. Zhou, T. Ando, and G. Shimaoka, *Electroluminescence*, S. Shionoya and H. Kobayashi, Editors, p. 65.
12. G. Zhou, Y. Nakanishi, and Y. Hatanaka, *Semicond. Sci. Tech.*, **7**, B549 (1992).
13. H. Yamamoto *et al.*, *Electron. Lett.*, **19**, 6 (1983).
14. C. N. Berglund and R. J. Powell, *J. Appl. Phys.*, **42**, 573 (1971).

Modeling of Plasma Etching Reactors Including Wafer Heating Effects

Eray S. Aydil*^a and Demetre J. Economou*

Department of Chemical Engineering, Plasma Processing Laboratory, University of Houston, Houston, Texas 77204-4792

ABSTRACT

A comprehensive mathematical model of chlorine etching of polysilicon in a single-wafer plasma reactor was developed from first principles. Wafer heat transport was included as an integral part of the analysis. The model provided the spatiotemporal variations of etchant concentration, wafer temperature, and etch rate. Under conditions of high etch rate and poor wafer cooling, etching was inherently transient. The polysilicon etch rate increased with time despite the fact that the atomic chlorine concentration decreased with time. This was due to wafer heating and the Arrhenius dependence of etch rate on temperature. Multichannel laser interferometry was developed to monitor the spatiotemporal variations of etch rate in real time. Measured etch rate transients compared favorably with model predictions. Results were sensitive to surface reaction parameters and to wafer back side cooling.

Plasma reactor modeling has received considerable attention recently in an effort to understand the intricate nature of the glow discharge and the plasma-wafer interaction.¹ Macroscopic plasma reactor models emphasize either the discharge structure² or transport and reaction of neutral species including the reaction rate distribution along the wafer surface.³ The latter models make the assumption of isothermal wafer. However, rapid reaction rates, ion bombardment, and/or poor heat transfer from the wafer can result in significant wafer heating which in turn can affect the etch rate, uniformity, and anisotropy.⁴ For example, Tachi *et al.*⁵ found a 80°C temperature rise during high rate etching of silicon. Wafer heating effects and etch rate transients are becoming increasingly important in plasma

etching as high input power and rapid etching are required to maintain high throughput in single-wafer machines. Theoretical studies of wafer heating to date examine the wafer in isolation from the rest of the reactor.⁶ This simplified approach is not adequate especially when chemical etching makes a contribution.

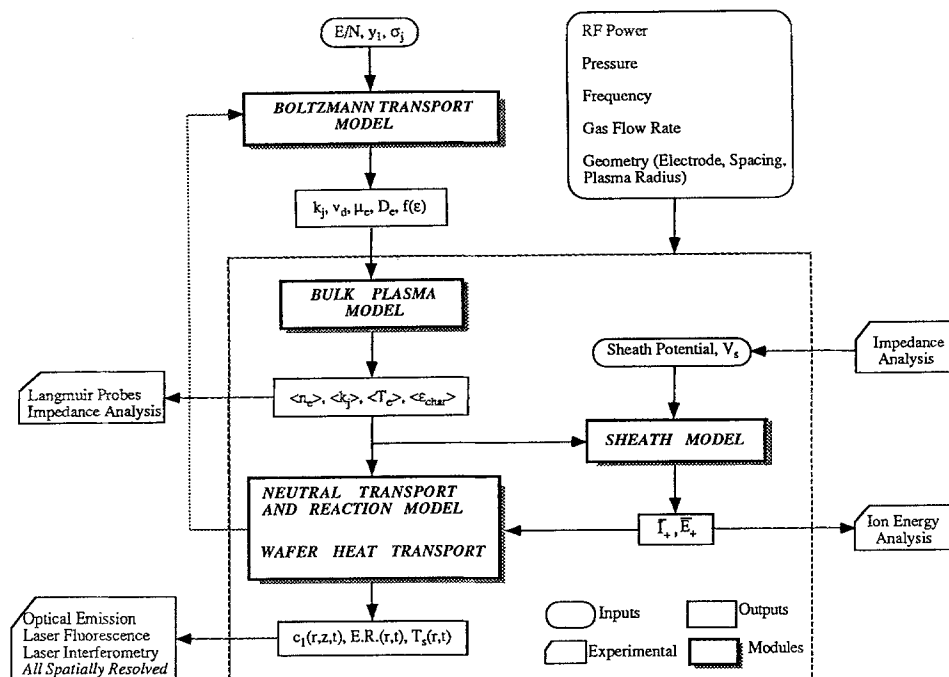
Recently, we developed a comprehensive model of a chlorine plasma sustained in a single-wafer reactor.⁷ The model was tested using a variety of plasma diagnostics. Electron density and energy, self-sustaining electric field, RF current flowing through the plasma, ion bombardment energy, and atomic chlorine concentration were found to agree with model predictions over a range of pressure, power, and electrode spacing without adjusting any reaction rate coefficients.

This model is expanded in the present work to include wafer heating as an integral part of the analysis. To our knowledge, this is the first model which considers the dy-

* Electrochemical Society Active Member.

^a Present address: Department of Chemical and Nuclear Engineering, University of California, Santa Barbara, CA 93106.

Fig. 1. Overview of modeling approach.



dynamic interaction of wafer heating with radical transport and reaction. The details of wafer heating are presented and experimental data on polysilicon etching using chlorine are compared to theoretical predictions. In comparison with the experimental data, the thermal accommodation coefficient on the back side of the wafer was the only adjustable parameter used. Multichannel laser interferometry was also developed to monitor the spatiotemporal variations of etch rate in real time.

Model Development

Integration of discharge physics and chemistry with radical transport and reaction in a self-consistent global plasma reactor model is a formidable task from the computational point of view. The work of Kushner and co-workers is a notable step towards this goal.⁸ Including wafer heating in a global reactor model complicates matters even further. This is due to the disparate time scales involved; plasma electrons respond on a nanosecond time scale whereas the wafer temperature changes on a time scale of minutes. To resolve this problem, a different approach was taken in modeling the glow discharge, whereby the inter-electrode space was divided into two regions: bulk plasma and sheath. This two-region approach was first taken to analyze etching of polymers in oxygen plasmas.⁹ However, the bulk plasma model used in the oxygen discharge work was greatly simplified. The two region approach was also followed in a more recent work⁷ which included a rather detailed bulk plasma model. In the present work, the model of Ref. 7 was extended further by including wafer heat transport. The advantage of the two-region approach is that it can be readily integrated with radical transport in the gas phase and heat transport in the semiconductor wafer.

A schematic of the modeling approach is depicted in Fig. 1, showing the different models, model inputs, and outputs. The Boltzmann transport equation was used to calculate the electron transport properties and electron-heavy particle reaction rate coefficients. These coefficients were parameterized and used in a bulk plasma model to calculate the self-consistent electric field, electron density, and electron energy. The bulk plasma model also provided the rate coefficients for radical production which were in turn used in a radical transport and reaction model. The latter was coupled with a model for wafer heat transport. The final output was the space and time variations of radical density, wafer temperature, and etch rate. In general the models are coupled with one another. For example, the rad-

ical transport and reaction model provides the gas composition which in turn affects the electron energy distribution function. The latter affects the electron impact reaction rate coefficients and therefore the plasma gas composition. In addition, the radical concentration is coupled to the wafer temperature. As the wafer temperature increases so does the etch rate resulting in stronger depletion of radicals.

A parallel plate reactor operating at relatively high pressure (0.25–2 Torr) and high frequency (13.56 MHz) was analyzed. Figure 2 shows a schematic of the reactor. The feed-stock gas enters the reactor uniformly through a showerhead electrode. The gas is dissociated into reactive radicals as the gas flows radially outwards. The radicals are transported by diffusion and convection, and participate in both homogeneous and heterogeneous reactions. The chlorine plasma etching of polysilicon was chosen to elucidate the coupling between electron kinetics, radical transport, and reaction and wafer heat transport. However, the general method of approach followed in this study may be applied to other plasma systems as well.

The models shown in Fig. 1 have been described previously,⁷ with the exception of the wafer heat transport model. Hence, in the following, details are omitted except for the latter model.

Boltzmann transport model.—The electron energy distribution function (EEDF) was obtained by solving the Boltzmann transport equation¹⁰

$$\left(\frac{\partial}{\partial t} + \mathbf{v} \cdot \nabla_{\mathbf{r}} - \frac{e\mathbf{E}}{m_e} \cdot \nabla_{\mathbf{v}}\right) f(\mathbf{r}, \mathbf{v}, t) = \left(\frac{\partial f}{\partial t}\right)_{\text{collisions}} = S \quad [1]$$

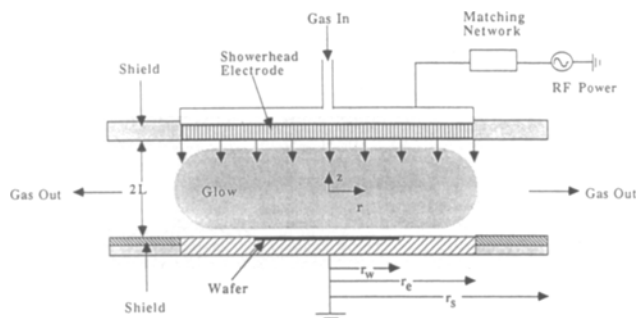


Fig. 2. Schematic of plasma reactor.

Table I. Important reactions in the chlorine discharge.

Electron impact reactions:		
Molecular ionization	$\text{Cl}_2 + e^- \rightarrow \text{Cl}_2^+ + 2e^-$	[R1]
Atomic ionization	$\text{Cl} + e^- \rightarrow \text{Cl}^+ + 2e^-$	[R2]
Dissociative attachment	$\text{Cl}_2 + e^- \rightarrow \text{Cl}_2^* \rightarrow \text{Cl} + \text{Cl}^-$	[R3]
Dissociative excitation	$\text{Cl}_2 + e^- \rightarrow \text{Cl}_2^*(\text{C}^1\Pi) + e^- \rightarrow 2\text{Cl} + e^-$	[R4]
Dissociative ionization	$\text{Cl}_2 + e^- \rightarrow \text{Cl}^+ + \text{Cl} + 2e^-$	
Electronic excitation	$\text{Cl}_2 + e^- \rightarrow \text{Cl}_2^*(\text{B}^3\Pi) + e^-$	
(Molecular chlorine)	$\text{Cl}_2 + e^- \rightarrow \text{Cl}_2^*(2^1\Pi \text{ and } 2^1\Sigma) + e^-$	
Vibrational excitation	$\text{Cl}_2 + e^- \rightarrow \text{Cl} \cdots \text{Cl}^* + e^-$	
Electronic excitations (six)	$\text{Cl} + e^- \rightarrow \text{Cl}^* + e^-$	
(Atomic chlorine)		
Other reactions:		
Ion-ion recombination	$\text{Cl}_2^+ + \text{Cl}^- \rightarrow \text{Cl}_2 + \text{Cl}$ $\text{Cl}^+ + \text{Cl}^- \rightarrow 2\text{Cl}$	
Volume recombination	$\text{Cl} + \text{Cl} + \text{M} \rightarrow \text{Cl}_2 + \text{M}$	[R5]
Wall recombination	$\text{Cl} + \text{Wall} \rightarrow 1/2 \text{Cl}_2 + \text{Wall}$	[R6]

The electric field to neutral density ratio, E/N , the plasma composition and a set of collision cross sections are needed as input to the Boltzmann equation to evaluate the collision integral, S , and the distribution function, f . Electron collision processes considered in this work are given in Table I. The isotropic EEDF f_0 was normalized using

$$\int_0^\infty \epsilon^{1/2} f_0(\epsilon) d\epsilon = 1 \quad [2]$$

Once the EEDF is calculated, a number of important quantities such as the electron drift velocity, rate coefficients for electron impact reactions, and the mean and characteristic electron energy can be computed. For example, the rate coefficient for the radical production reaction R4 of Table I is given by

$$k_j = \left(\frac{2e}{m_e}\right)^{1/2} \int_0^\infty f_0(\epsilon) \sigma_j(\epsilon) \epsilon d\epsilon \quad [3]$$

The rate coefficients were parameterized as a function of electric field and mole fraction of atomic chlorine and were used in the bulk plasma model described below.

Bulk plasma model.—The bulk plasma model relates the current flowing through the plasma to the electron kinetics. For a given set of operating conditions (see Fig. 1), the bulk plasma model predicts the time-dependent self-sustaining electric field and electron density. Once the electric field waveform is known, the time-dependent electron impact rate coefficients can be found, assuming that the EEDF follows the variations of the field. This assumption is reasonable since solutions of the time-dependent Boltzmann equation revealed that the rate coefficients for ionization and dissociation are fully modulated in time at an excitation frequency of 13.56 MHz.¹¹

The bulk plasma model was described by the following equations.

The electron balance

$$\frac{dn_e}{dt} = (k_{i1}y_1 + (k_{i2} - k_a)y_2)Nn_e - \frac{D_{ae}}{\Lambda^2} n_e \quad [4]$$

The terms on the right side of Eq. 4 account for electron production by atomic (rate coefficient k_{i1}) and molecular (k_{i2}) ionization, and electron loss by attachment (k_a) and diffusion, respectively. For the system used in this study the characteristic diffusion length is given by Eq. 5

$$\frac{1}{\Lambda^2} = \left(\frac{2.405}{r_e}\right)^2 + \left(\frac{\pi}{2L}\right)^2 \quad [5]$$

The total current balance

$$I_0 \sin(\omega t) = eAn_e v_d + \epsilon_0 A \frac{dE}{dt} \quad [6]$$

where $\omega = 2\pi\nu_a$. The peak current, I_0 , is related to the time-averaged power dissipated in the plasma by

$$\langle P_{RF} \rangle = \frac{2LI_0}{T} \int_t^{t+T} E(t) \sin(\omega t) dt \quad [7]$$

The above equations are solved for the steady-state electric field and electron density waveforms by knowing either the peak current I_0 or the time-averaged power dissipated in the plasma $\langle P_{RF} \rangle$. Due to the high resistivity of the bulk plasma in electronegative discharges, a large fraction of the power is dissipated in the bulk. The power dissipated in the sheaths can be estimated from experimental measurements of the ion bombardment flux and sheath voltage. For the conditions of this work, the power dissipated in each sheath was typically less than 10% of the total power and was neglected.

The rate coefficients for electron impact reactions (e.g., reaction R4 of Table I) are functions of time through their dependence on E/N . The time-average of a rate coefficient k_j was calculated by integrating over a period of the applied field

$$\langle k_j \rangle = \frac{1}{T} \int_t^{t+T} k_j(t) dt \quad [8]$$

The time-averaged rate coefficients were used in the radical transport and reaction model described below.

Neutral transport and reaction model.—The parallel plate plasma etcher shown in Fig. 2 is radially symmetric; hence a two-dimensional (r, z) model is sufficient to describe the fluid velocity, radical concentration, and etch rate profiles in the reactor. The momentum and mass balances were decoupled by assuming constant physical properties and negligible volume change upon reaction. Assuming that moderate variations in wafer temperature do not impact the gas physical properties significantly, the fluid velocity profile was considered time independent. In addition, the pressure was high enough for the continuum approximation to be valid.

The gas velocity distribution was found by solving the continuity and Navier-Stokes equations

$$\nabla \cdot \mathbf{u} = 0 \quad [9]$$

$$\rho_g \mathbf{u} \cdot \nabla \mathbf{u} + \nabla \cdot \boldsymbol{\tau} + \nabla P = 0 \quad [10]$$

The boundary conditions are

$$u = 0 \quad v = 0 \quad \text{at} \quad z = -L \quad \text{and} \quad 0 \leq r \leq r_s \quad [11]$$

$$u = 0 \quad v = -v_w \quad \text{at} \quad z = L \quad \text{and} \quad 0 \leq r \leq r_e \quad [12]$$

$$u = 0 \quad v = 0 \quad \text{at} \quad z = L \quad \text{and} \quad r_e \leq r \leq r_s \quad [13]$$

$$u = 0 \quad \frac{\partial v}{\partial r} = 0 \quad \text{at} \quad -L \leq z \leq L \quad \text{and} \quad r = 0 \quad [14]$$

$$u = u_{\max} \left(1 - \left(\frac{z}{L}\right)^2\right) \quad v = 0 \quad \text{at} \quad -L \leq z \leq L \quad \text{and} \quad r = r_s \quad [15]$$

where u and v are the radial and axial components of the velocity vector. The gas velocity at the showerhead v_w and the maximum velocity u_{\max} are given by

$$v_w = \frac{Q}{\pi r_e^2} \quad u_{\max} = \frac{3 v_w r_e^2}{8 L r_s} = \frac{3 Q}{8 \pi L r_s} \quad [16]$$

Equations 11 and 13 imply no slip on the walls, Eq. 12 is for a uniform gas entrance velocity at the showerhead electrode, and Eq. 14 is a result of radial symmetry. A well-developed parabolic velocity profile at the reactor exit was assumed, Eq. 15.

The atomic chlorine (etchant) mass balance was written as

$$\frac{\partial c_1}{\partial t} - D_1 \nabla^2 c_1 + \mathbf{u} \cdot \nabla c_1 - [(2k_a + k_a)n_e]c_2 + k_2 c_1^2 c_M = 0 \quad [17]$$

The atom concentration cannot respond to the rapid variations of the plasma excitation field. However, wafer temperature transients can have a time constant of the order of minutes. Since radical concentration is affected by wafer temperature, Eq. 17 includes a time dependent term to account for these transients.

The term in brackets in Eq. 17 is the time-averaged production rate coefficient of atomic chlorine calculated from Eq. 8. This term couples the Boltzmann transport model, bulk plasma model, and etchant transport and reaction model. It should be noted that the production rate coefficient is a function of atomic chlorine concentration c_1 since the EEDF depends on c_1 . Furthermore c_1 is a function of position in the reactor making the radical production rate coefficient spatially dependent. However, for small atomic chlorine mole fractions ($y_1 < 0.2$) the dependence of the radical production rate coefficient on c_1 is weak and its effects are secondary.⁷ Under this condition, the etchant production rate coefficient can be considered independent of position, and is then only a function of pressure, power, and reactor geometry. At relatively high pressure atomic chlorine is eliminated via the homogeneous recombination reaction R5 of Table I, where M is a third body. This reaction is represented by the last term on the left side of Eq. 17. The initial condition for Eq. 17 was taken as the steady-state concentration profile corresponding to a wafer temperature equal to the electrode temperature.

Etching and wall recombination reactions enter the model through the boundary conditions

$$\frac{\partial c_1}{\partial r} = 0 \quad \text{at} \quad r = 0, r = r_s \quad \text{and} \quad -L < z < L \quad [18]$$

$$-D_1 \frac{\partial c_1}{\partial z} - v_w c_1 = R_w(c_1) \quad \text{at} \quad z = L \quad \text{and} \quad 0 < r < r_e \quad [19]$$

$$-D_1 \frac{\partial c_1}{\partial z} = R_w(c_1) \quad \text{at} \quad z = L \quad \text{and} \quad r_e < r < r_s \quad [20]$$

$$D_1 \frac{\partial c_1}{\partial z} = R_w(c_1) \quad \text{at} \quad z = -L \quad \text{and} \quad 0 < r < r_s \quad [21]$$

where R_w is the wall recombination rate (reaction R6 in Table I) which depends on the wall material and surface condition. In this study a power law dependence was used, namely

$$R_w(c_1) = k_{mn} c_1^n \quad [22]$$

where k_{mn} is the n th order reaction rate constant for a surface material m . On surfaces undergoing etching boundary condition Eq. 21 is replaced by

$$D_1 \frac{\partial c_1}{\partial z} = R_w(c_1) + R_i(I_+, E_+, c_1) \quad \text{at} \quad z = -L \quad \text{and} \quad 0 < r < r_w \quad [23]$$

where the total etch rate R_i may contain an ion-assisted component which depends on the ion flux I_+ and mean ion energy E_+ . These quantities can be found from a sheath model.

Sheath model.—This model has been described before.¹² The dimensionless ion drift velocity is given by

$$(u_+^*)^2 = \frac{(-10V^*)^{2/5}}{(2Co)^{4/5}(1+2Co)^{1/5}} \quad [24]$$

where the collision number is $Co = 0.5N \lambda_D \sigma_i$, and the dimensionless variables are defined as follows

$$V^* = \frac{eV_s}{k_B T_s} \quad u_+^* = u_+ \sqrt{\frac{m_e}{k_B T_e}} \quad [25]$$

The sheath voltage is obtained from impedance measurements. The average ion bombardment energy was calculated from the drift velocity using

$$E_+ = \frac{1}{0.559} \left(\frac{1}{2} m_e u_+^2 \right) \quad [26]$$

Etching kinetics.—There are several UHV studies on etching of silicon with molecular chlorine under conditions simulating the plasma environment.^{13,14} In these studies the ion bombardment flux and energy and the Cl_2 flux were controlled separately. However, it is difficult to extrapolate these results to the relatively high pressure conditions of plasma etching. In the present study, the effect of ion bombardment was minimized by etching heavily P-doped polysilicon which is thought to etch chemically by Cl atoms. The relevant kinetics was recently investigated by Ogrzyzlo *et al.*;¹⁵ the etch rate is given by

$$E.R. (\text{\AA}/\text{min}) = 4.04 \times 10^{-18} N_D^{0.39} c_1 \sqrt{T_s} \exp\left(-\frac{E_a}{RT_s}\right) \quad [27]$$

where N_D is the dopant density and E_a is the activation energy. Equation 27 was adopted here to evaluate R_i assuming that the etching reaction produces $SiCl_4$ which is expected to be the major stable product at high pressure. The loss rate of atomic chlorine per unit area (in atom/cm²-s) is given by

$$R_t = 6.733 \times 10^{-28} \delta N_{Si} N_D^{0.39} \sqrt{T_s} \exp\left(-\frac{E_a}{RT_s}\right) c_1 \quad [28]$$

where δ is the number of chlorine atoms needed to remove a silicon atom (*i.e.*, $\delta = 4$ in this case) and N_{Si} is the atom density of silicon.

Wafer heat transport model.—As seen by Eq. 28, the etch rate depends exponentially on wafer temperature T_s . A modest temperature rise from 300 to 350 K causes the etch rate to increase by a factor of three. Several studies of wafer heat transport have been reported.¹⁶⁻¹⁸ However, modeling works to date consider the wafer in isolation and do not account for the coupling between the wafer temperature and radical transport.

Neglecting temperature variations along the thickness of the wafer, the wafer energy balance can be written as

$$\rho_{Si} C_{pSi} \frac{\partial T_s}{\partial t} = \kappa_{Si} \left(\frac{1}{r} \frac{\partial}{\partial r} \left(r \frac{\partial T_s}{\partial r} \right) \right) + \frac{Q_N}{\Delta} \quad [29]$$

where

$$Q_N = \frac{1}{2} k_{mn} c_{1s}^n \Delta H_r + \frac{1}{4} R_t \Delta H_e + I_+ E_+ - h_r (T_s - T_g) - h_B (T_s - T_c) - 2 \sigma_{SB} \epsilon_{Si} (T_s^4 - T_c^4) \quad [30]$$

In Eq. 29 the net heat flux to the wafer surface, Q_N , is divided by the surface to volume ratio (wafer thickness Δ) to accommodate the surface term into the one-dimensional model. In Eq. 30 the first two terms are heat generation due to surface recombination and etching, respectively, which are both exothermic reactions. The third term is the rate of energy transfer to the wafer via energetic ion bombardment. The fourth and fifth terms are the rates of energy loss from the wafer top and back side, respectively. The last term is the energy loss via radiation. Energy gain and loss mechanisms and model geometry are depicted in Fig. 3.

Boundary conditions are

$$\frac{\partial T_s}{\partial r} = 0 \quad \text{at} \quad r = 0 \quad [31]$$

$$-\kappa_{Si} \frac{\partial T_s}{\partial r} = h (T_s - T_g) \quad \text{at} \quad r = r_w \quad [32]$$

$$T_s = T_c \quad \text{at} \quad t = 0 \quad [33]$$

The no flux boundary condition at the center forces the solution to be symmetric. The initial wafer temperature was taken to be equal to the electrode temperature (Eq. 33). The latter was assumed to be kept constant by cooling water flow.

The wafer energy balance was solved simultaneously with the etchant mass balance Eq. 17. The ion flux I_i and energy E_i can be predicted by the sheath model or measured experimentally.⁷ These quantities are input into the wafer energy balance to determine the contribution of ion bombardment on wafer heating. For the relatively high pressure conditions examined here, ion bombardment contributed only 10-15% of the total heat flux.

The most important energy loss mechanism was found to be back side cooling. Both the electrode surface and the wafer back side are microscopically rough. The electrode and the wafer touch each other only at the top of the "hills" of their surface roughness as depicted in Fig. 3. Thus, there is a "gap" between the wafer and the electrode which is expected to be some tens of microns. At low pressures, at which the mean free path of gas species is much larger than the wafer-electrode gap, the heat transfer coefficient for back side cooling is independent of the wafer-electrode gap and is given by

$$h_B = \alpha_{acc} \Lambda_{Cl_2} P \quad [34]$$

where

$$\Lambda_{Cl_2} = \frac{1}{8} \frac{(\gamma + 1)}{(\gamma - 1)} \frac{1}{T_c} \sqrt{\frac{8k_B T_c}{\pi M_{Cl_2}}} \quad [35]$$

is the free-molecular heat conductivity.

When molecules strike a hot surface, complete interchange of energy does not occur at the first collision. Indeed, several collisions may be required before the molecule and the surface equilibrate. To take this effect into account, Knudsen introduced the accommodation coefficient, α_{acc} , which "can be defined as standing for the fractional extent to which those molecules that fall on the surface and are reflected or re-emitted from it have their mean energy adjusted or 'accommodated' toward what it would be if the returning molecules were issuing as a stream out of a mass of gas at the temperature of the wall." Accommodation coefficients have been measured or estimated for some systems.^{19,20} For very rough surfaces, the accommodation coefficient approaches one. Some attempts have been made to calculate the accommodation coefficient based on molecular collision and scattering concepts. A simple expression is¹⁹

$$\alpha_{acc} = \frac{2m_1 m_2}{(m_1 + m_2)^2} \quad [36]$$

where m_1 and m_2 are the mass of gas specie and surface atoms, respectively.

Heat transfer from the top side of the wafer was described by

$$-\kappa_g \left(\frac{dT_g}{dz} \right)_{z=L} = h_T (T_s - T_g) \quad [37]$$

The corresponding heat transfer coefficient can be shown to be

$$h_T = \frac{\kappa_g}{L} Pe_h \left(\frac{3}{16} + \frac{821}{26,880} Re \right) \frac{1}{\left\{ 1 - \exp \left[-Pe_h \left(\frac{3}{16} + \frac{821}{26,880} Re \right) \right] \right\}} \quad [38]$$

where $Pe_h = v_w \rho_g C_{pg} L / \kappa_g$, is the Péclet number for heat transfer and $Re = v_w L / 2\nu_g$, is the Reynolds number. It turns out that for typical conditions $Pe_h \ll 1$, and $Re \sim 1$. Hence the heat transfer coefficient can be approximated by κ_g / L , that is, for the low flow rates usually encountered in practice, conduction dominates convection heat transfer from the top of the wafer.

Method of Solution

The wafer energy balance Eq. 29 was solved in conjunction with the chlorine atom (etchant) mass balance Eq. 17 to compute the spatiotemporal variations of etchant concentration, wafer temperature and etch rate. The wafer energy balance was solved using the IMSL subroutine MOLCH which uses the method of lines with cubic Hermite polynomials. A simplified version of the wafer energy balance was also considered, namely, a steady-state spatially uniform temperature. In this case a continuation algorithm, DERPAR,²¹ was used to capture the multiple steady-states (see below).

The etchant mass balance Eq. 17 was also solved using the method of lines. The spatial derivatives were approximated by finite differences. The problem was then reduced to a set of time-dependent ordinary differential equations which were integrated with a modified version of the GEARB algorithm.

Substantial savings in computation time were realized by assuming that the etchant concentration profiles adjust rapidly in the variations of wafer temperature. This assumption is permissible since the etchant concentration responds on a time scale of 100 ms, whereas the wafer temperature responds on a time scale of minutes. The etchant mass balance was solved first using the initial wafer temperature. Next, the calculated concentration profile was used in the wafer energy balance to obtain the temperature distribution across the wafer surface for the first time interval, δt . This temperature profile was then used to obtain a new concentration profile. The calculation loop was repeated until the concentration and wafer temperature reached steady state or until a certain time period had elapsed. A value of $\delta t = 5$ s was found to be a good compromise between accuracy of computed results and CPU time requirements.

Experimental

The experimental system has been described elsewhere.⁷ Briefly, the plasma was sustained between two equal-area, 20.3 cm diam parallel plate electrodes with adjustable spacing. The temperature of both electrodes was controlled by a chiller/heater (Bay Voltex, Temptryte, HS-3500-WC-DC-SX). The chamber pressure was controlled by a closed-loop system consisting of a pressure transducer (MKS 222B), an exhaust throttle valve (MKS 253), and a controller (MKS 252A). Gas flows were regulated by mass flow controllers (Unit Instruments UFC-1100). Gases used were ultrapure chlorine, and prepurified argon used for actinometry. The etching chamber was pumped by a two-stage rotary vane mechanical pump (Edwards E2M40) with Fomblin oil service and an external oil filtration unit. A 600 l/s diffusion pump with a LN₂ trap (Edwards Diffstak CR160) was used to remove residual water vapor and achieve a background pressure of less than 10⁻⁶ Torr. Power was applied to the upper showerhead electrode by a 500 W, 13.56 MHz generator (RF Plasma Products RF5S). The actual power dissipated in the plasma was calculated from the product of the corrected current and voltage waveforms, accounting for stray impedance. Plasma emission was collected through a quartz side window and was transmitted to the entrance slit of a monochromator (Thermo Jarrell Ash Monospec 27). A diode-array detector (Princeton Instruments RY-1024 and ST-120 controller and PC

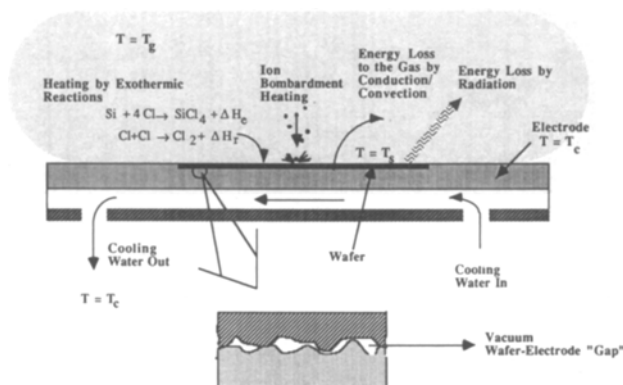


Fig. 3. Mechanisms of energy gain and loss by the wafer.

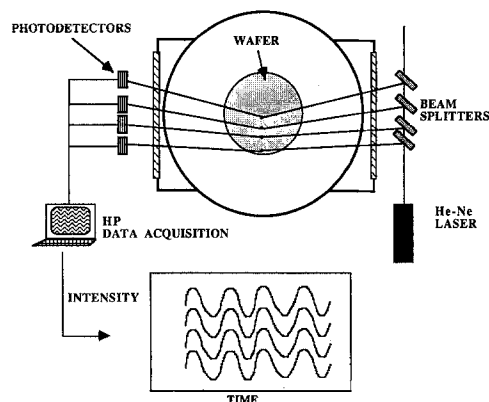


Fig. 4. Schematic of multichannel laser interferometer system.

data acquisition) was used to detect and record spectra. A small amount (5% by volume) of argon was added to serve as the actinometer gas.

The polysilicon etch rate was measured *in situ* using spatially resolved laser interferometry. This technique is an extension of conventional laser interferometry. The beam from a He-Ne laser (632.8 nm) was split into multiple beams (four in this study) using beam splitters. Each beam was directed at different radial positions on the wafer (Fig. 4). The reflected intensity from each position was monitored using silicon photodetectors. The etch rate as a function of position was calculated from the intensity variations. Etch rate transients were also captured. Multichannel laser interferometry provided a real time monitor of the spatiotemporal variations of etch rate. This technique is attractive for real time process monitoring and control.

The heavily P-doped polysilicon wafers used in this work were prepared by Texas Instruments Inc. The 100 mm diam wafers had a 1000 Å oxide layer under a 4600 Å polysilicon film. The poly was POCl₃ doped at 950°C for 20 min and deglazed in 10% HF solution for 1 min. The sheet resistance was $16 \pm 3 \Omega/\square$ corresponding to a dopant density of $1.3 \times 10^{20} \text{ cm}^{-3}$.

Etching of polysilicon in a chlorine plasma presents several problems. Previous researchers who have investigated this system noted inconsistencies and sporadic etching. These were attributed to the native oxide layer on silicon and the residual water vapor in the reactor. The polysilicon surface is covered with a native oxide a few tens of angstroms thick which does not etch with chlorine but can be sputtered by ions with energy exceeding ~50 eV.²² In the reactor used in the present work the ion bombardment energy was not sufficient to remove the native oxide. Hence, the oxide was removed using a short CF₄ pre-etch step similar to that used by Mogab and Levinstein.²³ Initiation of etching was monitored using laser interferometry. When CF₄ pre-etch was not used, polysilicon did not etch even after 45 min of plasma exposure. In contrast, the polysilicon film was found to clear within a few minutes if etching was initiated by removing the oxide.

Another problem with etching of polysilicon is formation of "black silicon" (sometimes known as "grass") under certain operating conditions. The formation of grass is attributed to "micromasking" by oxide which yields a rough surface. Roughening of polysilicon during etching has been recently investigated.²⁴ It was concluded that water vapor was responsible for this phenomena. Consistent with these studies, we found that a low base pressure (<10⁻⁵ Torr) in the etching chamber was necessary to etch polysilicon without forming black silicon. The etching chamber was thus evacuated with a diffusion pump for at least 12 h prior to an etching experiment.

Results and Discussion

Parameter values used for the results reported below are summarized in Table II. These values are used for calculations unless noted otherwise. The problem of wafer heating is discussed first followed by polysilicon etching and comparison with experimental data.

Wafer heating.—In order to gain some understanding of wafer heating, the wafer energy balance Eq. 29 was first solved independently from the etchant mass balance. In this case, the surface chlorine concentration becomes a free parameter. The steady-state spatially uniform wafer temperature was examined. The wafer temperature as a func-

Table II. Physical properties and parameter values.

Symbol	Name	Value
C_{pSi}	heat capacity of silicon	0.17 cal/g-K
C_{pR}	gas heat capacity	0.116 cal/g-K
D_{ae}	ambipolar diffusivity	$3.33 \times 10^6 \text{ cm}^2/\text{s}$
D_1	diffusion coefficient of Cl in Cl ₂	250 cm ² /s
E_a	etching reaction activation energy	4700 cal/mol
$k_{SS,2}$	2nd order surface recombination coeff. on SS	$3.1 \times 10^{-12} \text{ cm}^4/\text{s}$
$k_{Si,1}$	1st order surface recombination coeff. on Si	0 cm/s
k_{i1}, k_{i2}, k_d	electron-impact reaction coefficients	rate calculated through EEDF
k_a	attachment rate coefficient	rate calculated through EEDF
k_r	volume recombination coefficient	$9 \times 10^{-32} \text{ cm}^6/\text{s}$
N_D	dopant density	$1.3 \times 10^{20} \text{ cm}^{-3}$
N_{Si}	atomic density of silicon	$5 \times 10^{22} \text{ cm}^{-3}$
Q_c	gas flow rate	25 sccm
r_e	electrode radius	10.15 cm
r_s	shield radius	15.23 cm
r_w	wafer radius	5 cm
T^g	gas temperature	300 K
T_c^g	electrode temperature	293 K
v_w	gas velocity at the showerhead	1.073 cm/s
α_{acc}	thermal accommodation coefficient	0.41
ϵ_{Si}	emissivity of silicon	0.15
Δ	wafer thickness	0.05 cm
ΔH_r	heat of Cl-Cl recombination	57,300 cal/gmol
ΔH_c	heat of etching reaction	342,400 cal/gmol
κ_{Si}	thermal conductivity of silicon	0.358 cal/cm-s-K
κ_g	gas thermal conductivity	$1.78 \times 10^{-5} \text{ cal/cm-s-K}$
Λ_{Cl_2}	free molecular heat conductivity	0.0024 cal/cm ² -s-K-Torr
μ_g	gas viscosity	140 μP
ν_a	applied excitation frequency	13.56 MHz
ρ_{Si}	mass density of silicon	2.33 g/cm ³
ρ_g	gas mass density	$1.14 \times 10^{-6} \text{ g/cm}^3$

Note: Physical and transport properties are at 0.3 Torr and 300 K.

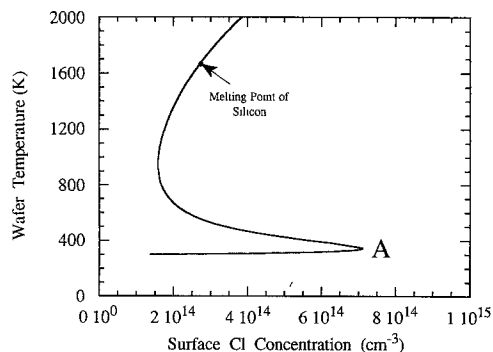


Fig. 5. Calculated steady-state wafer temperature as a function of surface chlorine atom concentration. Parameter values as in Table II.

tion of surface chlorine concentration shown in Fig. 5 exhibits multiple steady states (*i.e.*, more than one possible solutions at the same conditions). This type of behavior is well known (Ref. 25, see also references therein) and arises from the Arrhenius temperature dependence of the etching rate (Eq. 28). It is noted that the diagram shown in Fig. 5 was obtained for realistic parameter values. Based on the behavior of similar systems,²⁵ the upper and lower branches in Fig. 5 are expected to be stable while the middle branch is expected to be unstable. Any value of the surface concentration beyond the limit point A will drive the system towards the upper branch of very high temperature. Of course, the upper branch is not reachable in practice since the melting point of silicon is only 1688 K. In practice, any reasonable thickness of polysilicon film would clear rapidly as the temperature (and hence etch rate) rises, thereby preventing large excursions in temperature.

The most important consequence of this multiplicity, however, is that a steady-state wafer temperature may never be reached during etching. For example, when the conditions are such that the upper branch is the only solution (say for a surface chlorine concentration of $8 \times 10^{14} \text{ cm}^{-3}$) etching of any practical thickness of polysilicon film will be inherently transient. A steady-state temperature (and etch rate) cannot be reached before the film clears.

One should note at this point that coupling the etchant mass balance (Eq. 17) to the wafer energy balance has a stabilizing effect in the sense that as the wafer temperature and etch rate increase, the wafer becomes a stronger sink for Cl and the reaction eventually becomes diffusion limited. In other words, the surface Cl concentration would decrease as the etch rate rises (see also Fig. 9 below).

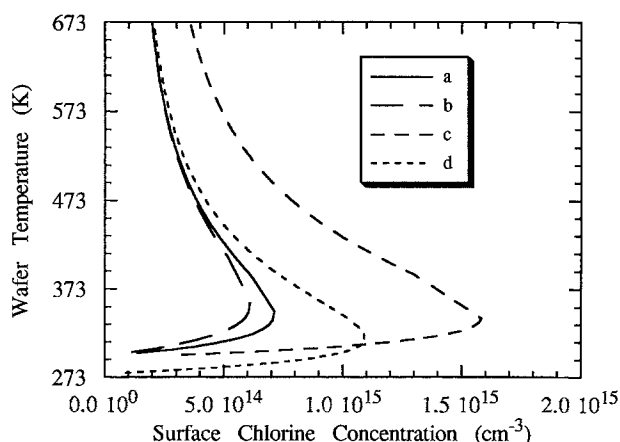


Fig. 6. Calculated steady-state wafer temperature as a function of surface chlorine atom concentration. a, As in Fig. 5; b, $\alpha_{acc} = 0.41$, $T_c = 293$, $k_{Si,1} = 1000 \text{ cm/s}$; c, $\alpha_{acc} = 1$, $T_c = 293$, $k_{Si,1} = 0 \text{ cm/s}$; and d, $\alpha_{acc} = 0.41$, $T_c = 273$, $k_{Si,1} = 0 \text{ cm/s}$.

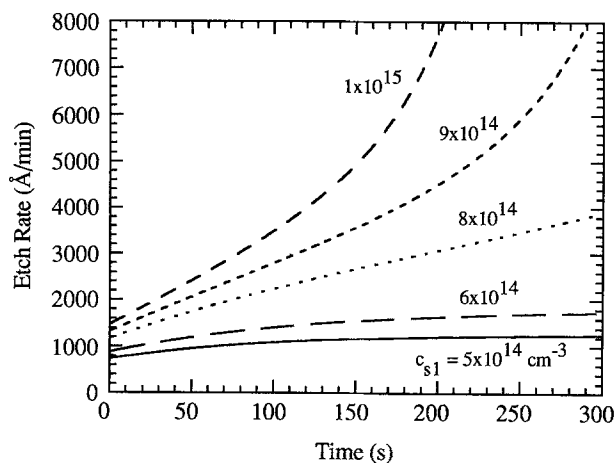


Fig. 7. Calculated etch rate transients for the conditions of Fig. 5.

Figure 6 shows the steady-state wafer temperature as a function of the surface Cl concentration for a realistic temperature range. The sensitivity of wafer temperature to the values of surface recombination coefficient on silicon, thermal accommodation coefficient, and coolant temperature are shown. Curves a and b were computed using recombination coefficients, $k_{Si,1} = 0$ and 1000 cm/s , respectively. This range of surface recombination coefficient covers the range of reaction probability $\gamma_s \approx 0-0.1$. The additional heat produced by surface recombination reduces the value of the limit point chlorine concentration, albeit by a small amount (curve a to curve b). One concludes that the steady-state wafer temperature is not very sensitive to the surface recombination coefficient. In contrast, the wafer temperature is very sensitive to the thermal accommodation coefficient and the coolant temperature (curves c and d). This is because back side cooling is the major mechanism of heat loss from the wafer.

Figure 7 shows the transient behavior of etch rate for different atomic chlorine surface concentrations. The etch rate reaches a steady state for concentrations less than $6 \times 10^{14} \text{ cm}^{-3}$ but “runs away” for higher concentrations (above the limit point). It takes several minutes to reach the steady state when such a state exists. Otherwise, etching is transient for the whole duration of the process. The wafer temperature is most likely to run away when the heat produced by the etching reaction is high (for high chlorine surface concentration, high dopant density, intense ion bombardment) and/or the rate of heat removal is low (poor wafer back side contact, low thermal accommodation coefficient, substrate electrode not cooled).

Runaway phenomena can occur for any exothermic etching process if the heat of reaction is high enough.⁴ Another candidate for runaway is etching of photoresist in an oxygen discharge. Curiously, under certain conditions (high RF power, insufficient back side cooling) photoresist films have been observed to “char.”

For the cases studied, most of the energy deposited on the wafer is produced by the etching reaction and is lost by back side cooling. For example, for a surface concentration of $6 \times 10^{14} \text{ cm}^{-3}$ and at steady state (Fig. 7), 85% of the total energy gained by the wafer is produced by the etching reaction; ion bombardment accounts for the remaining 15% (surface recombination was neglected in this case). If a modest value (say $k_{Si,1} = 100 \text{ cm/s}$) is used for the surface recombination coefficient on silicon, recombination is the second highest energy production mechanism after etching. Referring still to Fig. 7, the energy loss by back side cooling is 80% of the total. Radiation accounts for 12.5%, and the remaining 7.5% is lost from the top surface of the wafer by conduction. The total steady-state energy flux to the wafer is 0.0422 W/cm^2 which corresponds to 3.3 W for a 100 mm diam wafer.

The wafer heating results discussed so far were for a spatially uniform surface Cl concentration. The time- and space-dependent wafer energy balance was also solved by using different atomic chlorine surface concentration profiles as input. Three profiles were used

(i) Constant

$$c_{1s}(r) = c_{1s0} \quad [39]$$

(ii) Parabolic decreasing towards the wafer edge

$$c_{1s}(r) = c_{1s0} \left(1 - \left(\frac{r}{r_w} \right)^2 \right) \quad [40]$$

(iii) Parabolic increasing towards the wafer edge

$$c_{1s}(r) = c_{1s0} \left(\frac{r}{r_w} \right)^2 \quad [41]$$

For case (i) the temperature was constant across the wafer and rose as a function of time. For cases (ii) and (iii) the radial temperature distribution was nonuniform. However, when the surface concentration level was low (low c_{1s0}), the temperature between the wafer center and edge was within a few degrees K. When the surface chlorine concentration was high enough to cause runaway, there were marked temperature gradients between the center and edge of the wafer. As an example, Fig. 8 shows the time evolution of the temperature profile across the wafer for a parabolic chlorine concentration decreasing towards the wafer edge and with $c_{1s0} = 2 \times 10^{15} \text{ cm}^{-3}$. At the early stages of etching the radial temperature distribution is uniform to within a few K. As the temperature rises, the center of the wafer (where the chlorine concentration is highest) starts to runaway first and the temperature gradients increase to as many as 10–15 K across the wafer radius. While a temperature difference of 10 K may not seem large, this would cause a 20% nonuniformity in etch rate, which is intolerable in practice. Similar results were obtained when the chlorine surface concentration profile was of the form of Eq. 41. The wafer temperature followed the shape of the concentration profile decreasing towards the center.

Polysilicon etching.—Results from the complete reactor model are shown next. The wafer energy balance Eq. 29

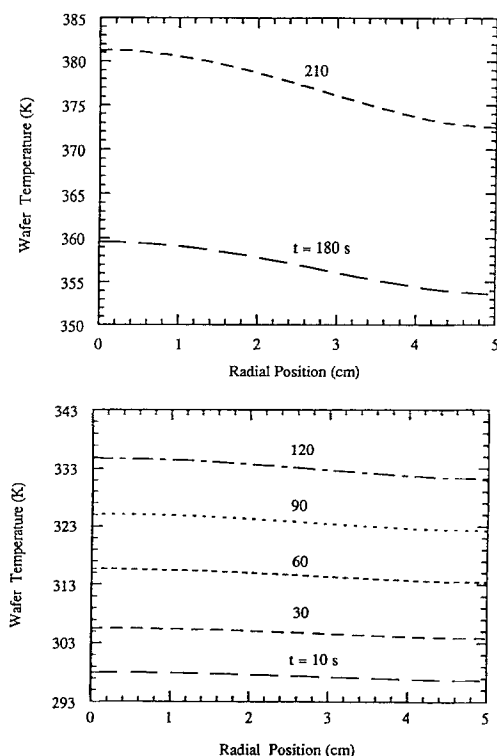


Fig. 8. Calculated spatiotemporal variation of wafer temperature. Surface Cl concentration profile as in Eq. 40 with $c_{1s0} = 2 \times 10^{15} \text{ cm}^{-3}$.

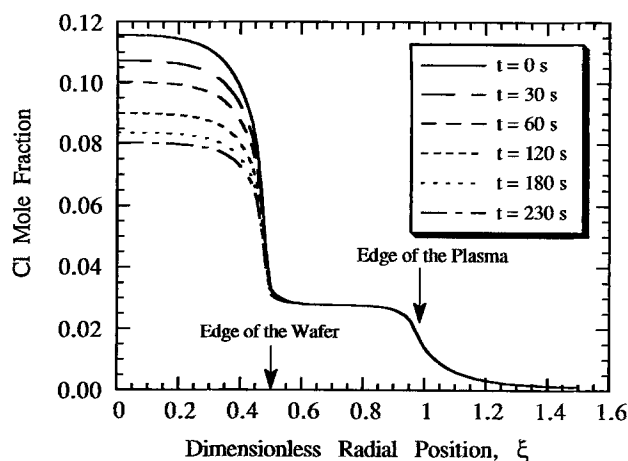


Fig. 9. Calculated spatiotemporal variation of atomic chlorine concentration. Parameter values as in Table II.

was solved in conjunction with the etchant mass balance, Eq. 17, to calculate the spatiotemporal concentration, etch rate, and wafer temperature profiles.

Figure 9 shows the radial distribution of atomic chlorine surface concentration as a function of time for the basic conditions (Table II). The concentration increases towards the wafer center because the wafer surface was assumed to be less reactive towards atomic chlorine than the surrounding stainless steel electrode surface.²⁶ Under these conditions the wafer temperature (not shown) was relatively uniform and increased with time due to heat released by the etching reaction. The increase in wafer temperature enhanced depletion of Cl over the wafer causing a decrease in atomic chlorine concentration with time. The transients over the surrounding electrode ($0.5 < \xi < 1.0$) are much weaker because the surface recombination coefficient ($k_{ss,2}$ Table II) was taken independent of temperature. The atomic chlorine concentration drops further beyond the edge of the plasma since atoms are produced only within the plasma zone.

Figure 10 shows that the concentration profiles change drastically by using a silicon surface recombination coefficient of $k_{si,1} = 1000 \text{ cm/s}$. Other parameters were as in Fig. 9. The atomic chlorine concentration is now increasing monotonically towards the wafer edge; this is because of the increased reactivity of the wafer as compared to that of the surrounding electrode. This is also the reason for the overall reduction in atomic chlorine concentration, as compared to Fig. 9. Furthermore, the atomic chlorine concentration is now a weak function of time because surface recombination is the predominant loss mechanism of Cl,

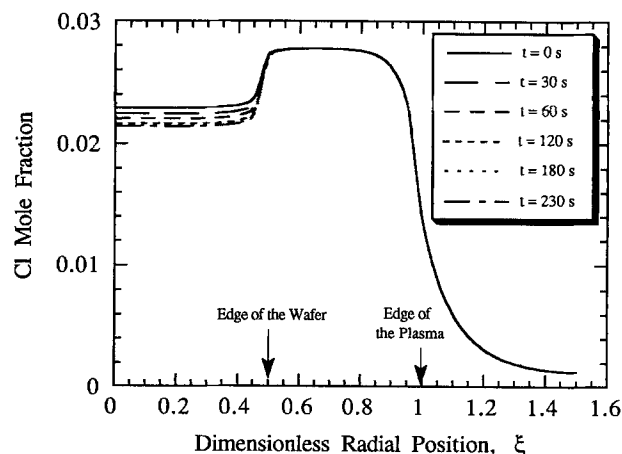


Fig. 10. Calculated spatiotemporal variation of atomic chlorine concentration. Parameter values as in Table II except that $k_{si,1} = 1000 \text{ cm/s}$.

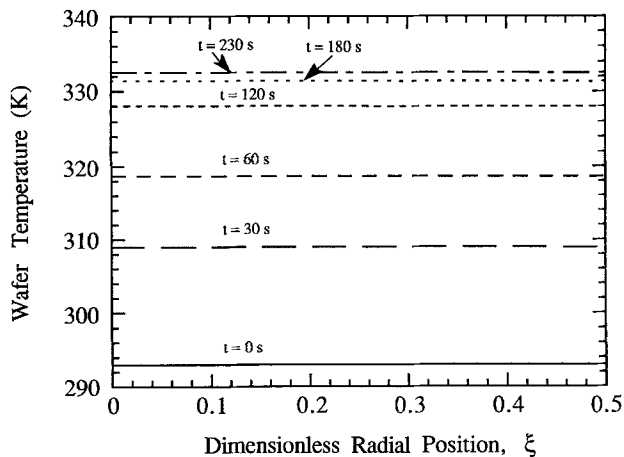


Fig. 11. Calculated spatiotemporal profiles of wafer temperature for the conditions of Fig. 10.

and the corresponding coefficient was assumed independent of temperature.

Although the transients in atomic chlorine concentration are weak, the wafer temperature and etch rate vary considerably with time (Fig. 11 and 12). What is striking is that the etch rate increases by a factor of three in less than 4 min, despite the fact that the etchant concentration decreases during the same period. This is a direct consequence of wafer heating. The temperature profiles are relatively flat, and the etch rate profiles follow the shape of the atomic chlorine concentration.

Experimental data and comparison with theory.—Figure 13 shows the space and time resolved etch rate of polysilicon for 50 W (nominal power), 0.3 Torr, 25 sccm, and 2.54 cm electrode spacing. The actual power dissipated in the plasma was 39 W. The spatiotemporal variations of etch rate were monitored in real time using spatially resolved laser interferometry.²⁷ The atomic chlorine concentration as a function of time (the ratio of 808.7 nm Cl emission to 811.5 nm Ar emission) is also shown in Fig. 13. The etch rate increases drastically with time despite the fact that the atomic chlorine concentration decreases somewhat during etching (from start of etching to point A). The wafer edge etches faster than the wafer center. The edge starts clearing 220 s after the plasma is turned on (point A in Fig. 13). At this time the atomic chlorine concentration in the reactor starts rising. Points B, C, and D indicate the times at which the film clears to radial positions of 28, 12, and 0 mm (wafer center), respectively. As the film edge starts clearing and the atomic chlorine concentration rises, the etch rate increases even more rapidly (see etch rate at $r = 28$ mm after point A, for example). This increase in etch rate is partly due to an increase in Cl concentration in the reactor due to

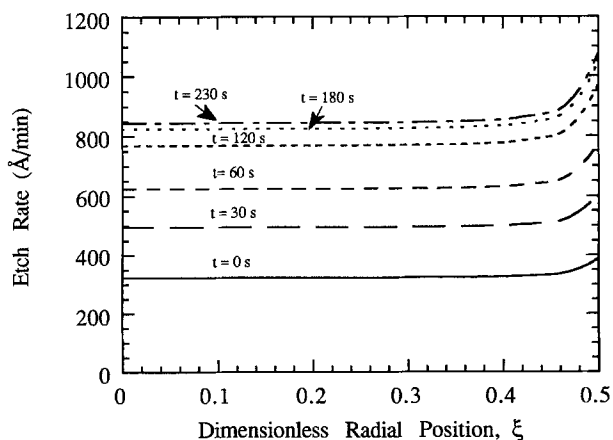


Fig. 12. Calculated spatiotemporal profiles of etch rate for the conditions of Fig. 10.

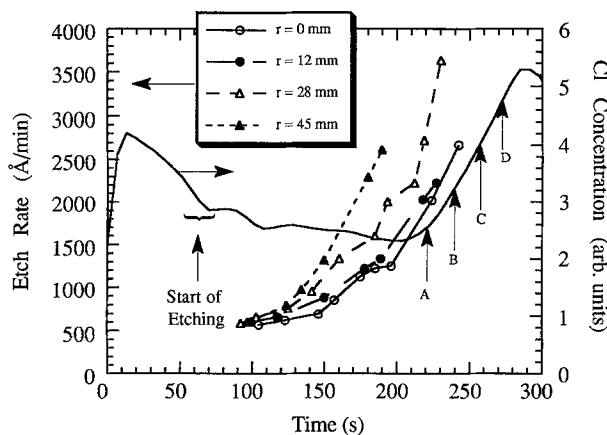


Fig. 13. Measured spatiotemporal profiles of polysilicon etch rate for 50 W, 0.3 Torr, 25 sccm, and 2.54 cm electrode spacing. Atomic chlorine concentration transient (as measured actinometrically) is also shown. Other parameter values as in Table II.

the following reason: the Cl reactivity on oxide is much lower than that on polysilicon. As the polysilicon film clears and the underlying oxide is exposed the atomic chlorine concentration rises due to loading. The plasma characteristics do not change appreciably during etching. Indeed, the emission intensity from the Ar 811.5 nm line rose a modest 10% as the polysilicon film was clearing indicating only a slight change in the electron energy distribution function and/or electron density. The increase in etch rate before wafer edge clearing (before point A in Fig. 13) cannot be attributed to loading. Since both the Cl and Ar emission line intensities remained relatively constant during this period and since heavily P-doped polysilicon is known to etch chemically, the increase in etch rate is due to an increase in wafer temperature.

The qualitative behavior seen in Fig. 13 was reproducible and was also observed under different operating conditions. For example, for 100 W of power, the etch rate rose from 1000 to 6000 Å/min in less than 1 min. The transient was more severe as compared to Fig. 13 because of the higher power loading resulting in increased heat dissipation on the wafer. The hypothesis of etch rate acceleration due to wafer temperature rise was checked by another experiment. Instead of placing the wafer on the bare stainless steel electrode, a thin coating of a heat sink compound (Dow Corning Compound 340) was applied to the back side of the wafer. The etch rate was lower and the transients were much milder than without the heat sink. Also, etching uniformity was improved dramatically.

Comparison of the experimentally measured etch rate with the theoretically predicted value was difficult because there is no kinetic information on Cl reactions with polysilicon surfaces in a plasma. Ogryzlo *et al.*¹⁵ studied the kinetics of polysilicon etching with Cl atoms in the absence of ion bombardment. In these experiments, the polysilicon sample was placed downstream of a plasma. This is in contrast to the present study, where the polysilicon was exposed to the plasma. Despite this difference, the kinetic expression reported by Ogryzlo *et al.* (Eq. 27) was used here as a reasonable first approximation.

Figure 14 shows the comparison between the experimental (points) and theoretical (lines) etch rate at the wafer center as a function of time. Model predictions are shown for two different thermal accommodation coefficients, α_{acc} , which was the only adjustable parameter in the model. In order to compare theory to experiment, the initiation period required to remove the oxide (as determined by laser interferometry) was subtracted from the real time. The etch rate is higher for the lower thermal accommodation coefficient because the wafer temperature is then higher. The model captures the initial transient as well as the magnitude of etch rate satisfactorily considering the uncertainty in the kinetic expression used. The increase in etch

rate after ~ 120 s cannot be captured by the model in its present form. This increase is due to loading as the poly film is clearing and progressively more of the underlying oxide is exposed to the plasma (the reactivity of Cl on oxide is much lower than that on poly). A rather simple modification of the model can capture this effect.

It was further found that the model predictions were sensitive to the etching reaction activation energy. It appears that better understanding of surface chemistry is important for enhancing the predictive abilities of the model. In practice, one can adjust the values of the thermal accommodation, surface recombination, and etching reaction coefficients to fit the experimental data. Such fitting was not attempted here because the use of many adjustable parameters was not desirable.

Summary and Conclusions

A comprehensive mathematical model of chlorine etching of polysilicon in a single-wafer plasma reactor was developed from first principles. A modeling methodology was outlined which can be applied to other plasma systems as well. Solutions to the Boltzmann equation provided the electron transport and reaction coefficients. The glow discharge was modeled by dividing the interelectrode space into bulk plasma and sheath. The glow discharge model provided the self-sustaining electric field, electron density and energy, ion bombardment flux and energy, and radical production rate coefficients. The latter were input to neutral transport and reaction equations coupled to a wafer heat transport equation. Spatiotemporal variations of etchant concentration, wafer temperature, and etch rate were thus computed.

As a result of the temperature dependence of etch rate, the wafer temperature can have multiple values for the same set of parameters. Under conditions of high etch rate and poor wafer cooling, etching was inherently transient. The energy released by the exothermic etching reaction and back side cooling were found to be the most important energy gain and loss mechanisms, respectively. The situation may be different in high density plasma reactors (*e.g.*, ECR) where ion bombardment can be the main mechanism for wafer heating. The wafer temperature distribution was relatively flat except for cases of strongly nonuniform radical concentration profiles across the wafer surface. The shape of the temperature distribution was then found to follow the radical concentration distribution.

The polysilicon etch rate increased with time despite the fact that the atomic chlorine concentration decreased with time. This was due to wafer heating and the Arrhenius dependence of etch rate on temperature. Uniformity of etching depended on the relative reactivity (against Cl atoms) of the wafer surface compared to that of the surrounding elec-

trode surface. A novel technique was developed, based on laser interferometry, to monitor *in situ* the transients in etch rate and uniformity. Measured etch rate transients compared favorably with model predictions. However, model predictions were sensitive to the surface reaction parameters. Thus, better knowledge of surface kinetics is essential for enhancing the predictive capabilities of the model.

Additional *in situ* process diagnostics would provide more rigorous tests of the model predictions. For example, laser induced fluorescence (LIF) can provide spatially resolved atomic chlorine concentration profiles near the wafer surface,²⁸ where they are needed most. Unfortunately, optical emission spectroscopy cannot be used within the sheath because there are too few electrons to provide atomic excitation. Besides, the assumptions of actinometry may be violated in the sheath. Also, it would be interesting to monitor the wafer temperature in real time. IR laser interferometry as described by Donnelly and McCauley²⁹ appears to be a good choice. One of the main advantages is that this method is nonintrusive. From the practical point of view, however, one is interested in measuring directly the etch rate and its uniformity. The multichannel laser interferometric technique provides a real time monitor of both etch rate and uniformity. Sensors such as this are invaluable for process control of plasma reactors.

Acknowledgments

The authors thank the National Science Foundation (CBT 8708908), Texas Instruments, Inc., the Welch Foundation, and the Texas Advanced Research Program for financial support of this work. We are grateful to Dr. Gabe Barna, Dr. Lee Lowenstein, and Dr. Wayne Fisher of Texas Instruments for providing technical support.

LIST OF SYMBOLS

A	electrode area, cm^2
c	species concentration, cm^{-3}
c_1	atomic chlorine concentration, cm^{-3}
c_2	molecular chlorine concentration, cm^{-3}
c_M	concentration of third body, cm^{-3}
c_{s1}	surface concentration of atomic chlorine, cm^{-3}
C_{pg}	gas heat capacity at constant pressure, J/g-K
C_{pSi}	silicon heat capacity at constant pressure, J/g-K
Co	collision number
D	diffusion coefficient, cm^2/s
D_{ae}	electron ambipolar diffusion coefficient, cm^2/s
E, E_e	electric field, V/cm
E_a	etching reaction activation energy, J/mol
E_+	ion bombardment energy, eV
e	electronic charge, $1.609 \cdot 10^{-19} \text{ C}$
f	electron velocity distribution function
f_0	isotropic electron energy distribution function
h_B	heat transfer coefficient for back side cooling, $\text{J/cm}^2\text{-K-s}$
h_T	top-side heat transfer coefficient, $\text{J/cm}^2\text{-K-s}$
I_0	peak current, A
I_+	ion bombardment flux, A/cm^2
k_a	dissociative attachment reaction rate constant, cm^3/s
k_B	Boltzmann's constant, eV/K
k_d	molecular chlorine dissociation rate constant, cm^3/s
k_{i1}	atomic chlorine ionization rate constant, cm^3/s
k_{i2}	molecular chlorine ionization rate constant, cm^3/s
k_{mn}	n th order reaction rate constant for a surface material m , $\text{cm}^{(3n-2)}/\text{s}$
k_r	homogeneous (volume) recombination rate constant, cm^6/s
L	half interelectrode gap, cm
m_e	electron mass, g
m_+	ion mass, g
N	total neutral density, cm^{-3}
N_D	dopant density, cm^{-3}
N_{Si}	atom density of silicon, cm^{-3}
n_e	electron density, cm^{-3}
P	pressure, Torr
$\langle P_{RF} \rangle$	time-average RF power, W
Q, Q_0	volumetric flow rate, cm^3/min , sccm
Pe_h	Péclet number for heat transfer

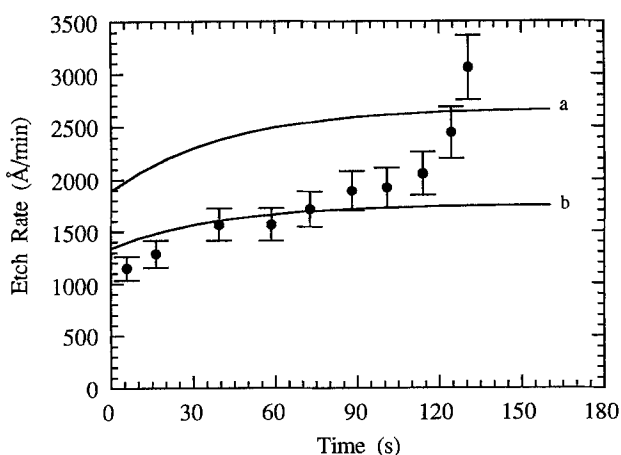


Fig. 14. Comparison of calculated (lines) and measured (points) transients of polysilicon etch rate. Curve a is for $\alpha_{occ} = 0.50$ and curve b is for $\alpha_{occ} = 0.75$. Conditions were 100 W, 0.5 Torr, and 1.27 cm electrode spacing. Other parameter values as in Table II.

Re	Reynolds number
R	universal gas constant, 8.307 J/mol-K
R_t	total etch rate, $\text{cm}^{-2} \text{s}^{-1}$
R_w	wall recombination reaction rate, $\text{cm}^{-2} \text{s}^{-1}$
r	radial position, cm
r_e	electrode radius, cm
r_s	shield radius, cm
r_w	wafer radius, cm
S	collision integral
T	period of the applied field, s
T_c	coolant temperature, K
T_e	electron "temperature," K
T_g	gas temperature, K
T_s	wafer temperature, K
t	time, s
u	gas velocity vector, cm/s
u	radial component of the gas velocity vector, cm/s
u_z	ion drift velocity in the sheath, cm/s
u_z^*	dimensionless ion drift velocity in the sheath
v	electron velocity vector, cm/s
V^*	dimensionless sheath potential drop
V_s	sheath potential, V
v	axial component of the gas velocity vector, cm/s
v_d	electron drift velocity, cm/s
v_w	gas velocity at the showerhead electrode, cm/s
y	species mole fraction
z	axial position, cm
Greek	
α_{acc}	thermal accommodation coefficient
γ	ratio of heat capacities, C_p/C_v
δ	number of chlorine atoms reacting per silicon atom
Δ	wafer thickness, cm
ΔH_r	heat of recombination, J/mol
ΔH_e	heat of etching, J/mol
ϵ	electron energy, eV
ϵ_{Si}	emissivity of silicon
ϵ_0	vacuum permittivity, $8.854188 \times 10^{-12} \text{ J}^{-1} \text{ C}^2 \text{ m}^{-1}$
κ_g	thermal conductivity of gas, J/cm-s-K
κ_{Si}	thermal conductivity of silicon, J/cm-s-K
Λ	characteristic diffusion length, cm
Λ_{Cl_2}	free-molecular heat conductivity of chlorine, J/cm ² -s-K-Torr
ν_g	gas kinematic viscosity, cm ² /s
ν_a	applied excitation frequency, $\omega/2\pi$, s ⁻¹
ρ_g	gas density, g/cm ³
ρ_{Si}	silicon density, g/cm ³
σ_i	collision cross section for electron impact reaction j, cm ²
σ_{SB}	Boltzmann constant
τ	shear stress tensor
ω	applied excitation frequency, $2\pi\nu_a$, rad/s
∇_x, ∇_r	gradient in the x, y, z space
∇_v	gradient in the velocity space

REFERENCES

- L. Kline and M. J. Kushner, *Crit. Rev. Solid State Mater. Sci.*, **16**, 1 (1989).
- See *IEEE Trans. Plasma Sci.*, April (1991) and articles therein.
- S.-K. Park and D. J. Economou, *This Journal*, **137**, 2624 (1990); M. Dalvie and K. F. Jensen, *J. Vac. Sci. Technol. A*, **8**, 1648 (1990).
- J. C. Martz, D. W. Hess, and W. E. Anderson, *J. Appl. Phys.*, **67**, 3609 (1990).
- S. Tachi, K. Tsujimoto, S. Arai, and T. Kure, *J. Vac. Sci. Technol. A*, **9**, 796 (1991).
- B. C. Dems and F. Rodriguez, *J. Vac. Sci. Technol. B*, **8**, 1985 (1990).
- E. S. Aydil and D. J. Economou, *This Journal*, **139**, 1396, 1406 (1992); *ibid.*, **139**, 1396 (1992).
- T. J. Sommerer and M. J. Kushner, *J. Appl. Phys.*, **71**, 1654 (1992).
- D. J. Economou and R. C. Alkire, *This Journal*, **135**, 2786 (1988).
- W. L. Morgan, Report 19, Joint Institute for Laboratory of Astrophysics, University of Colorado, Boulder, CO (1979).
- J. Ping and D. J. Economou, *J. Appl. Phys.*, Accepted.
- D. J. Economou, D. R. Evans, and R. C. Alkire, *This Journal*, **135**, 756 (1988).
- J. Dieleman, F. H. M. Sanders, A. W. Kolfshoten, P. O. Zalm, and A. E. DeVries, *J. Vac. Sci. Technol. B*, **3**, 1384 (1985).
- S. E. McNevin and G. E. Becker, *ibid.*, **3**, 485 (1985).
- E. A. Ogryzlo, D. E. Ibbotson, D. L. Flamm, and J. A. Mucha, *J. Appl. Phys.*, **67**, 3115 (1990).
- A. Durandet, O. Joubert, J. Pelletier, and M. Pichot, *ibid.*, **67**, 3862 (1990).
- R. J. Cantolini, *This Journal*, **135**, 929 (1988).
- M. Nakamura, T. Kurimoto, H. Yano, and K. Yanagida, in *Dry Process*, J.-i. Nishizawa, Y. Horiike, M. Hirose, and K. Sato, Editors, PV 88-7, p. 78, The Electrochemical Society Softbound Proceedings Series, Pennington, NJ (1988).
- S. Dushman, in *Scientific Foundation of Vacuum Technique*, 2nd ed., J. M. Lafferty, Editor, John Wiley & Sons, Inc., New York (1962).
- E. H. Kennard, *Kinetic Theory of Gases*, McGraw-Hill, Inc., New York (1938).
- M. Kubicek and M. Marek, *Computational Methods in Bifurcation Theory and Dissipative Structures*, Springer-Verlag, New York (1983).
- W. M. Holber and J. Foster, *J. Vac. Sci. Technol. A*, **8**, 3720 (1990).
- C. J. Mobag and H. L. Levinstein, *ibid.*, **17**, 721 (1980).
- D. J. Thomas, P. Southworth, M. C. Flowers, and R. Greef, *J. Vac. Sci. Technol. B*, **8**, 1044 (1990).
- D. Luss, *Chem. Eng. Ed.*, 12 (1986).
- D. J. Economou, S. K. Park, and G. D. Williams, *This Journal*, **136**, 188 (1989).
- E. S. Aydil and D. J. Economou, *J. Appl. Phys.*, **69**, 109 (1991).
- G. S. Selwyn, L. D. Baston, and H. H. Sawin, *Appl. Phys. Lett.*, **51**, 898 (1987).
- V. Donnelly and J. McCaulley, *J. Vac. Sci. Tech. A*, **8**, 84 (1990).